LANGMUIR Article
Cite This: Langmuir 2018, 34, 4811−4819
pubs.acs.org/Langmuir

Cluster Assemblies Produced by Aggregation of Preformed Ag Clusters in Ionic Liquids

Stefanie Roese,[†] Alexander Kononov,[†] Janis Timoshenko,[‡] Anatoly I. Frenkel,[‡,¶] and Heinz Hövel*[,†]

[†]Fakultät Physik/DELTA, Technische Universität Dortmund, 44227 Dortmund, Germany
[‡]Department of Materials Science and Chemical Engineering, Stony Brook University, Stony Brook, New York 11794, United States
[¶]Division of Chemistry, Brookhaven National Laboratory, Upton, New York 11973, United States

Supporting Information

ABSTRACT: Room-temperature ionic liquids (RTILs) can be used as electrosterical stabilizers for nanoparticles without adding stabilizing agents. However, the nanoparticle stability and its mechanisms are still in discussion. We deposited preformed 2 nm ±0.6 nm silver clusters into the ionic liquid $C_4MIM\ PF_6$ using in situ UV/vis absorption to monitor the deposition process. The time- and temperature-dependent cluster aggregation process was studied with ex situ UV/vis absorption spectroscopy analyzed with electrodynamic calculations using generalized Mie theory. On an atomistic level, the sample structure was investigated using EXAFS and a neural network based analysis of XANES. The combination of all methods shows that an aggregation of the original 2 nm clusters without coalescence takes place, which can be controlled or stopped by choosing an appropriate sample temperature. This approach allows the controlled production of chainlike cluster aggregates in RTIL, promising for a number of applications.

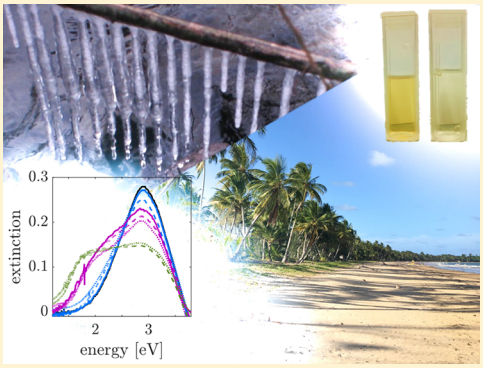

INTRODUCTION

Nanoparticles have attracted tremendous attention because of their unique properties, used, for example, in catalysis[1] or as sensors.[2] Plasmonic materials like silver or gold nanoparticles can be used for optical sensing or as active plasmonic devices.[3] Because of their unsaturated surface, nanoparticles tend to lower their surface to volume ratio by aggregation and, finally, coalescence to larger particles. With the coalescence to larger particles, the advantageous properties of the nanoparticles by definition mitigate or disappear.

To fight aggregation the nanoparticles can be embedded into a solid material, for example, a polymer,[4,5] or they can be separated by ligand shells.[6] However, this usually weakens the nanoparticle properties related to their large active surface, such as the catalytic activity. Templated surfaces can be used to fix bare nanoparticles at defined positions,[7−9] but the amount of material produced by this method is limited by the two-dimensionality of the substrate; even if this can be partly overcome by stacking these structures.[10] In addition, the nanoparticle properties are often significantly changed by the interaction with the surface. For example, they are flattened, in the extreme case, to atomic layers.[11]

However, contrary to coalescence to large particles, a nanoparticle aggregation without coalescence may lead to useful effects. The formation of conductive paths in the resulting nanoscopic network structure can be of interest for applications.[12,13] For certain metals as, for example, silver or gold plasmonic hot spots[14,15] at the contact spots between the aggregated nanoparticles play an important role in surface-enhanced Raman scattering[16,17] or for the production of hot electrons with applications in photocatalysis and solar energy conversion.[18] For such samples, a controlled aggregation without coalescence has to be combined with a detailed analysis of the resulting aggregates. We show here that preformed nanoparticles deposited into an ionic liquid are most suitable and practical in this context.

Room-temperature ionic liquids (RTILs) are salts with a melting point below room temperature, which have proven to serve as efficient stabilizers for nanoparticles without the need of adding stabilizing agents by exploiting both electrostatic and steric properties of RTILs.[19] In contrast to common solvents, they offer advantages like a negligible vapor pressure, high thermal and chemical stability, and a large electrochemical window depending on their composition.[20] Several methods for the fabrication of ionic-liquid stabilized nanoparticle samples have been reported. Besides chemical synthesis by hydrogen reduction of metal compounds,[21,22] samples can physically be fabricated by sputter deposition[23−25] or by physical vapor deposition.[26] A detailed review on the different sample production methods is given by Dupont and Scholten.[27] However, no consensus concerning sample stability and stabilizing mechanisms, which are crucial for possible applications, has been reached yet.[28] Although some groups[29−31] report long-term stable samples, other groups do

Received: November 20, 2017
Revised: February 27, 2018
Published: March 22, 2018

DOI: 10.1021/acs.langmuir.7b03984
Langmuir 2018, 34, 4811−4819

not obtain stable samples without the addition of stabilizing agents.[32−34] All these groups are using ionic liquids as both solvent and stabilizer, which complicates the discussion of sample stability since the processes of nanoparticle formation from individual atoms and simultaneous particle aggregation cannot be detected separately.[35]

We recently presented a new approach of sample production by depositing preformed 2 nm Ag clusters with a narrow size distribution into the ionic liquid 1-butyl-3-methylimidazolium hexafluorophosphate by using a custom-built mixer enabling in situ UV/vis absorption measurements.[36] We use the term "cluster" instead of "nanoparticle" to address separated particles of well-defined size. Using this technique we skip the phase of nanoparticle formation inside the ionic liquid and by the in situ optical spectroscopy we verify that the particles stay separated during the deposition process. Thus, we are able to assign every change in the sample afterward to aggregation.

In this paper, we present a systematic study on the aggregation of RTIL stabilized Ag clusters by the combination of several complementary methods. Time- and temperature-dependent ex situ UV/vis absorption spectroscopy as a fast and versatile method is analyzed with electrodynamic calculations using Generalized Mie Theory. The atomistic sample structure and structural changes during aggregation were investigated using EXAFS and a neural network based analysis of XANES, providing, in particular, access to coordination numbers, which can be linked to particle sizes.[37,38] The combination of all methods shows that an aggregation of the original 2 nm clusters without coalescence takes place. It can be controlled or stopped by choosing an appropriate sample storage temperature. The controlled production of chainlike aggregates of 2 nm clusters in RTIL is promising for many applications.

SAMPLE PRODUCTION

The ionic liquid 1-butyl-3-methylimidazolium hexafluorophosphate $C_4MIM\ PF_6$ was purchased from IoLiTec and was dried for 6 h at 90 °C under vacuum conditions to remove the water.[35] Afterward it was transferred into the UHV chamber, where 2 nm ± 0.6 nm Ag clusters are produced in a supersonic expansion[39] with a rate of 9 μg/min (measured with a quartz crystal balance). 130 μg Ag clusters in total are deposited into 15 mL of ionic liquid, which is filled in a rotating mixer. Details on the deposition process of preformed Ag clusters have been introduced in our previous publication.[36]

UV/VIS ABSORPTION SPECTROSCOPY

Two fused silica windows at both sides of the mixer (optical path length of 6 cm) enable in situ UV/vis absorption measurements during deposition to control the cluster plasmon during the deposition process. Cluster plasmons are collective oscillations of the conduction electrons.[40] The resonance position and shape of the cluster plasmon of a separated cluster depends on the interaction between the cluster and the RTIL. The used cluster apparatus is one of the few examples, where the optical spectra of the free cluster beam in vacuum could be measured for the same clusters as deposited into embedding media.[39] It may be even the only example using direct optical absorption for the free beam clusters as contrasted, for example, to depletion techniques. This can be employed for a surface analysis by cluster plasmon spectroscopy of the separated clusters as reported in the previous publication.[36] The setup for the optical spectra of the free cluster beam in vacuum could not be used in combination with the in situ optical measurements for the deposition into the RTIL here, but the cluster source is identical and the optical spectra in the free beam proved to be the same in a large number of experimental runs. In contrast, XANES and EXAFS spectra of the free cluster beam in vacuum were impossible to be measured with the cluster apparatus used here.

If the clusters aggregate, they couple electromagnetically, which becomes apparent in a broadened or splitted cluster plasmon with a shifted resonance position. This can be utilized to investigate the aggregation process.[3]

All optical measurements were performed using an Avantes AvaLight-DH-S-BAL light source providing wavelengths in the range of λ = 190−2500 nm and an Avantes AvaSpec 2048 × 14 spectrometer with a resolution of $\Delta\lambda$ = 1.4 nm and a spectral range of λ = 200−1100 nm. During the deposition we used the in situ spectroscopy to cross-check the amount of silver clusters deposited and to ensure that the clusters stayed separated during the time of the deposition experiment.[36] After the cluster deposition is finished, the sample is removed from the UHV chamber and filled into 1 cm fused silica or PMMA cuvettes for ex situ UV/vis absorption measurements to investigate the sample stability.

TEMPERATURE-DEPENDENT CLUSTER AGGREGATION

The sample changed its apparent color as a function of time and temperature from a strong yellow to gray. Using ex situ UV/vis absorption spectroscopy the cluster plasmon was investigated. The absorption of $C_4MIM\ PF_6$ in the UV spectral range limits the usable spectral range to 1.1−3.8 eV. Figure 1

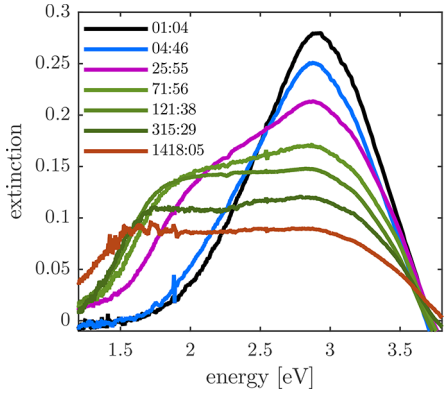

Figure 1. Sample aggregation during storage at 277 K. Legend denotes time in hours and minutes as HH:MM after sample deposition.

shows the aggregation process during storage at 277 K. The corresponding storage times ("hours:minutes") are given in the legend. Immediately after deposition, a strong plasmon at 2.91 eV is visible ("phase 1", black line). After a few hours, the extinction at 2.91 eV decreases ("phase 2", blue line). After 1 day, the extinction further decreases, while simultaneously there is an increase of the extinction at lower energies ("phase 3", purple line). On a time scale of several days, there is a second point of inflection ("phase 4", green lines). Afterward the overall extinction decreases until no plasmon can be detected anymore ("phase 5", brown line). These phases describe the gradual formation of cluster aggregates, whose morphology will be discussed below. In a much later stage (not shown here) the clusters precipate, explaining the gradually diminishing

DOI: 10.1021/acs.langmuir.7b03984
Langmuir 2018, 34, 4811−4819

extinction. The broadening of the cluster plasmon resonance and the increase of the extinction at lower energy can be assigned to sample aggregation (see below).

To analyze the structure of the aggregates, electrodynamic calculations based on the Generalized Mie Theory[41] have been performed using the Python-based software *py_gmm*,[42] which has been validated by comparing the results to calculations performed by Quinten.[43] The *py_gmm* code is able to model far- as well as local-field spectra of arbitrary formed cluster aggregates for all incident field polarizations. For the simulations an Ag cluster diameter of 2 nm, the dielectric function of silver[44] corrected by chemical interface damping[39] with $A = 1$, and a dielectric function of the surrounding medium of $n = 1.75$ were chosen. These parameters describe the separated clusters immediately after deposition similar to the results in our previous publication.[36] The interparticle distance was set to 0.05 nm, which means that the clusters are touching, but still without coalescence.

Figure 2 shows the results obtained for different shapes of aggregates. The black line in Figure 2c) shows the cluster plasmon of a single 2 nm Ag cluster. In Figure 2a) a compact aggregate formed by the packing of 13 clusters in the form of a cuboctahedron (black line) is compared to a linear chain of 13 clusters (red line). The pronounced low energy shoulder positioned at approximately 1.5 eV is only observed for the linear chain. For the dimer formed by two clusters also shown in Figure 2a) (green line) this shoulder is less pronounced.

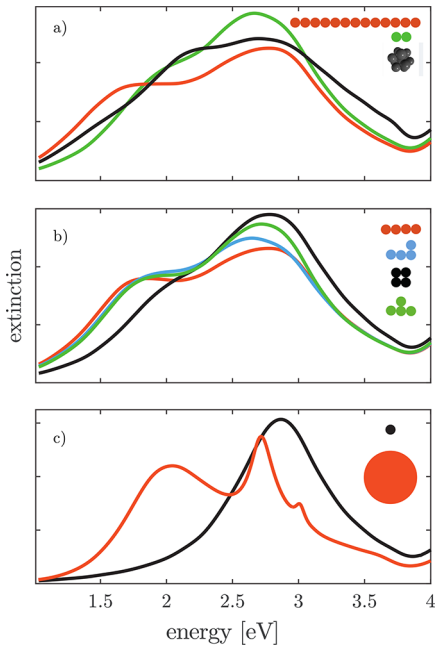

Figure 2. Extinction spectra for different aggregate morphologies calculated using the *py_gmm* code. (a) Comparison between a dimer (green), a cuboctahedron (black) and a linear chain (red), the latter two consisting of 13 clusters. (b) Comparison of planar 4-cluster aggregates as suggested by Quinten,[45]. (c) Single 2 nm cluster (black) and a 40 nm cluster (red). See text for the discussion of the different aggregates.

The comparison of different aggregates consisting of four clusters as suggested by Quinten[45] is shown in Figure 2b). We find the largest peak splitting with a pronounced low energy shoulder for linear or branched aggregates, while for the more compact cubic aggregate (black line) the peak splitting is very small.

To explain our energy flank of the spectra at about 1.5 eV in an alternative model with separated larger clusters formed by coalescence of the original 2 nm clusters a diameter of approximately 40 nm has to be assumed (Figure 2c), red line). But this interpretation can be excluded, considering the EXAFS results (see below).

A UV/vis absorption measurement always averages over different shapes and sizes of aggregates, and a mixture of aggregates and separated clusters is present, in particular at the beginning of the aggregation process. Therefore, the exact morphology in each aggregation phase cannot be defined. Each phase consists of a mixture of still single clusters and aggregates of different size. Nevertheless the calculations in Figure 2 show that the pronounced low-energy shoulder in the experimental spectra can only be explained with the large splitting of the resonances caused by linear aggregates formed by the original 2 nm sized clusters.

A visualization of the cluster aggregates and determination of their shape using transmission electron microscopy (TEM) is not possible for clusters stabilized in ionic liquids because the extraction of the clusters into a volatile solvent may compromise the TEM results due to uncontrollable aggregation processes,[46] which was shown for one example in our previous publication.[36]

The speed of the aggregation process can be varied by keeping the sample at different temperatures. Therefore, the sample was split up and filled into four cuvettes that were stored at different temperatures: at room temperature (293 K), in a refrigerator (277 K), in a freezer (253 K), and in liquid nitrogen (77 K). Because the viscosity of ionic liquids increases dramatically with decreasing temperature,[47] it is expected that the Brownian motion will be slowed down. The temperature- and time-dependent measurements are shown together with pictures of the visual appearance of the samples after 24 h in Figures S1 and S2, respectively. Figure 3 compares the spectra taken for the samples stored at different temperatures (solid lines, room temperature; dashed lines, refrigerator; dotted lines,

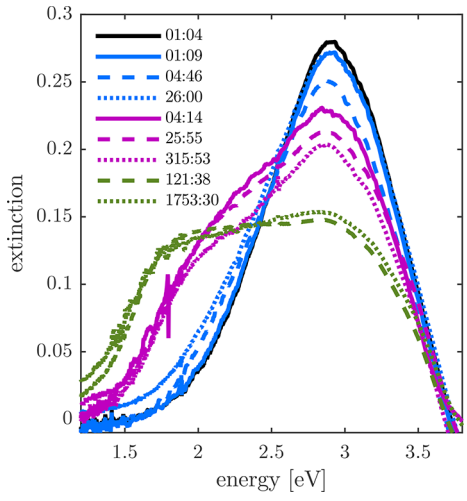

Figure 3. Sample storage at different temperatures: at room temperature (293 K, solid lines), in a refrigerator (277 K, dashed lines), and in a freezer (253 K, dotted lines). The colors denote the different aggregation phases (see text). The times in the legend are given in hours and minutes as HH:MM after sample deposition.

DOI: 10.1021/acs.langmuir.7b03984
Langmuir 2018, 34, 4811−4819

freezer). The entries in the legend denote the time in "hours:minutes" after deposition. The different colors in Figure 3 represent different phases of aggregation as described for the refrigerator measurement introduced above in the discussion of Figure 1. For the sample stored at room temperature, only spectra of the phases 2 and 3 could be recorded, because 24 h after the deposition, no plasmon could be detected anymore (cf. the visual appearance of the samples in the Figure S2). Note that the time scales of the different temperatures vary widely, which proves the significant enhancement of sample stabilization at low temperatures.

To evaluate the kinetics of the aggregation process, the times for the phases at different temperatures shown in Figure 3 are presented in an Arrhenius plot (Figure 4).

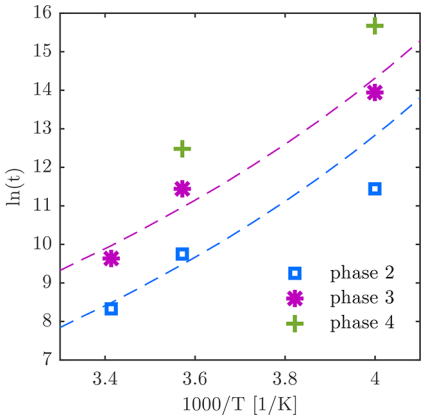

Figure 4. Description of the aggregation phases 2 and 3 by using a model for diffusion-limited coagulation taking into account the temperature dependence of the ionic liquid viscosity.

An activation energy can be calculated using the relation

$$k = A\exp\left(-\frac{E_A}{k_B T}\right) \tag{1}$$

$$\ln(t) = \text{const.} + \frac{E_A}{k_B}\frac{1}{T} \tag{2}$$

For the calculation of the activation energy only the data points taken for sample storage at room temperature and in the refrigerator have been taken into account because the time scale of the sample stored in the freezer is already affected by the time at room temperature necessary for sample defrosting before each optical measurement. The calculation yields activation energies of E_A = 0.7 and 0.9 eV for the phases 2 and 3, respectively. However, we do not think that interaction limited aggregation is the apt model for the highly viscous RTIL here. Instead we use an alternative semiquantitative explanation based on the temperature dependent model for the collision frequency $\tau = \nu^{-1}$ for diffusion limited coagulation introduced by Kraynov et al.[19] and inserting the slightly extrapolated data for the temperature dependent viscosity $\eta(T)$ of C_4MIM PF_6 given by Harris et al.[47] The number of collisions a cluster experiences per time unit is given by

$$\nu(T) = \frac{kT}{\pi\eta(T)R^3}\phi \tag{3}$$

with cluster radius R = 1 nm and volume fraction $\phi = 9.5 \times 10^{-7}$. The experimental data can be described (dashed lines in Figure 4) by choosing only one free fit parameter, the temperature independent coagulation probabilities of $1/(1.6 \times 10^4)$ and $1/(7 \times 10^4)$ for the phases 2 and 3, respectively. This suggests that the viscosity is the main contributing effect concerning sample stability. The model of diffusion limited coagulation with a temperature independent coagulation probability is reasonable because of the comparably small temperature range.

The largest part of the sample was stored in liquid nitrogen (77 K), however, we show no spectra for different storage times since this storage temperature is below the glass transition temperature T_g = 197 K of C_4MIM PF_6.[48] At this temperature the clusters stay separated for virtually infinite duration. After warming to room temperature the optical spectra were identical to those before cooling and no changes of the cluster plasmon could be observed after storage at 77 K several months after deposition. This allows, e.g., the transport of samples to synchrotron radiation facilities. We used this to analyze the atomistic sample structure and structural changes during aggregation by X-ray absorption spectroscopy.

X-RAY ABSORPTION SPECTROSCOPY

X-ray absorption fine structure (XAFS) spectroscopy is a widely used tool for studies of the local structure around X-ray absorbing atoms. The absorption coefficient for X-rays is measured in the vicinity of the absorption edge as a function of the incident photon energy, which can be translated in terms of the energy of excited photoelectrons. Within 30 eV below to ca. 1000 eV above the excitation energy of the core electrons, also known as the X-ray absorption edge energy E_0, the X-ray absorption coefficient exhibits fine structure. It is caused by both the nonmonotonic energy dependence of the (unoccupied) electronic density of states and the interference between the outgoing and scattered photoelectron waves that can be constructive or destructive, depending on the photoelectron wavelength and thus incident X-ray energy. Because of the sensitivity to the electronic structure and relative positions of neighboring atoms to the X-ray absorbing atom, the 3D geometry of the absorbing atom environment is encoded in the XAFS spectrum.

The XAFS spectrum has two parts that contain complementary information: X-ray absorption near edge structure (XANES) that corresponds to the region from ca. 30 eV below the absorption edge to 40 eV above, and extended X-ray absorption fine structure (EXAFS), that extends ca. 1000 eV or further past the edge.

EXAFS is commonly used to determine the coordination numbers and interatomic distances in metallic particles.[37] The EXAFS signal can be represented as a sum of the contributions χ_i originating from the photoelectron backscattering from the i-th shell:

$$\chi(k) = \sum_i \frac{S_0^2 n_i}{kR_i^2} f_i(k)\sin\left[2kR_i - \frac{4}{3}C_{3,i} + \delta_i(k)\right] e^{-2\sigma_i^2 k^2} e^{-2R_i/\lambda_i(k)} \tag{4}$$

Here $k = \sqrt{2m(E - E_0)/\hbar^2}$ denotes the photoelectron wavenumber, $f_i(k)$ is the photoelectron scattering amplitude, $\delta_i(k)$ is the phase, S_0^2 is the amplitude reduction factor, n_i is the degeneracy of the scattering path (equal to the coordination number for single scattering paths), R_i is the effective half-path length (equal to the interatomic distance for single scattering

DOI: 10.1021/acs.langmuir.7b03984
Langmuir 2018, 34, 4811−4819

paths), σ_i^2 is the Debye−Waller factor which characterizes the mean-square relative displacements of atoms, $C_{3,i}$ is the third cumulant of the pair distribution function and λ_i is the photoelectron effective mean free path.[49]

Parameters n, R, σ^2, and C_3 can be obtained from the nonlinear least-squares fitting of experimental EXAFS data with eq 4. Here we limit our analysis to the contribution from the first coordination shell only.

While EXAFS analysis is widely used for studies of nanomaterials, it has significant limitations. First, eq 4 is valid only for systems with moderate bond length disorder, where the bond-length distribution can be described with a quasi-Gaussian function. Thus, it works well for bulk-like materials, but not for small nanoparticles, where the shapes of bond-length distributions can be more complex, e.g., asymmetric. Failure to account for these disorder effects in EXAFS analysis may result in significantly underestimated coordination numbers, disorder factor values and interatomic distances, as demonstrated in refs 37 and 50−53. Second, good quality data up to 10 Å^{-1} or more in the wavenumber (k) space are required for reliable EXAFS analysis, which are not always available, especially in the cases of in situ experiments and diluted systems. The XANES signal also contains information about the nearest bonding environment around the absorbing atom, and XANES spectra do not suffer from the same data quality limitations as EXAFS. However, this structural information is hidden in the XANES spectra and cannot be extracted via fitting with an analytical equation, as in EXAFS analysis. Therefore, we complement here EXAFS analysis with a recently developed neural network (NN) based analysis of XANES data. Sensitivity of XANES features to particle size and shape was acknowledged before,[54−56] but just recently a method was developed that allows quantitative analysis of XANES spectra in metallic particles.[38] In this approach for the interpretation of XANES data, an artificial neural network is used, which is a complex function in multidimensional space that maps the discretized XANES spectrum to a set of structure descriptors, such as the coordination numbers of nearest neighboring atomic shells around the absorber. These coordination numbers are averaged over the intra- and interparticle distribution of bonds, just as in the case of EXAFS analysis. The parameters of this function are optimized using a training data set, which is a large set of XANES spectra, for which the true values of structure descriptors (coordination numbers) are known. To construct such a training data set, we rely on ab initio XANES simulations with FEFF9[57] and FDMNES[58] codes for a set of nanoparticle models with different shapes and sizes. In details the NN-based approach for XANES analysis is described in ref 38.

All XAFS experiments have been carried out at beamline P64 at DESY, Hamburg. The incident energy is tuned with a liquid nitrogen cooled double crystal monochromator with Si(111) and Si(311) reflections. An ionization chamber filled with krypton is used to determine the intensity of the incident beam. X-ray absorption was measured in fluorescence mode by scanning from 200 eV below to 500 eV above the Ag K edge (25.514 keV). The Ag K_α fluorescence is detected by a 100 pixel Ge detector from Canberra Industries perpendicular to the incident beam to suppress contributions from elastic scattering.

The sample is filled into a sample holder with a thickness of 1.6 cm corresponding to the absorption length of C_4MIM PF_6 containing 2 mL of the sample. The sample holder is sealed with Kapton windows. The sample is placed in a custom built cell, which is temperature controlled using a circulation thermostat. The cell can be evacuated using a membrane pump or flushed with dry nitrogen gas to avoid water condensation at the cell windows. The sample temperature is controlled by two thermocouples.

After measuring an Ag reference foil, a sample precharacterized with UV/vis spectroscopy containing separated Ag clusters is filled into the sample holder. The X-ray absorption spectrum is recorded at 250 K to avoid sample aggregation during the measurement. Afterward the sample is warmed up to room temperature and the aggregation process is controlled using UV/vis spectroscopy for 2.5 h. After this time the sample changed its state from separated to aggregated, which could also be seen in a change of the sample color from yellow to gray. The sample was then cooled again to 250 K in order to avoid further aggregation. To ensure that no radiation damage affects the structure of the ionic liquid stabilized clusters during the long time, in which the sample was exposed to the X-rays, we performed a control experiment with the same sample aggregation monitored by UV/vis spectroscopy without any previous X-ray exposure.

XAFS DATA PREPARATION

Because the fluorescence line of interest strongly overlaps with the tail of the scattering line,[59] the Ag K_α fluorescence line is extracted from the total fluorescence spectrum using a modified Gaussian peak fitting algorithm[60] instead of setting a region of interest at the Ag K_α fluorescence line. This significantly improves the signal-to-noise ratio, which is of crucial importance, especially for the EXAFS analysis.

Before the analysis of XAS data the background was removed and the spectrum was normalized via standard procedure.[49,61] EXAFS data fitting was performed by LARCH,[62] FEFF-9,[57] and IFEFFIT[63] codes. Fitting of EXAFS data for the Ag foil was used to determine the values of nonstructural parameters S_0^2 and ΔE_0, a correction to the photoelectron origin.

XAS RESULTS

The k^2-weighted EXAFS data are shown in Figure 5. The reduced amplitude of the fine structure oscillations of the cluster samples compared to the spectrum taken for the Ag foil is consistent with the expected reduced coordination number. For analysis the $\chi(k)$ data were Fourier transformed in the k range between 3 and 9 Å^{-1}. Fitting of the first coordination shell EXAFS data was performed in the R-space between 1.2 and 3.0 Å (Figure 6).

The resulting fits for all spectra are given in Table 1. A coordination number n_1 of 9.2 ± 0.9 was obtained for the sample containing separated clusters. This value is in accordance with the coordination number expected for the cluster size of 2 nm either obtained by model calculations[64] or in experimental studies.[65,66] This corroborates the results obtained from UV/vis spectroscopy, showing that the deposited preformed clusters stay separated after deposition as well as during storage in liquid nitrogen. Also no significant change in the coordination number of both aggregated samples can be observed within the experimental error bar (10.6 ± 1.1 and 9.0 ± 1.4, respectively). All measured coordination numbers are found to be well below the value for the bulk fcc structure (12). This excludes the aggregation to significantly larger particles, whose XAS spectra will look identical to an Ag

DOI: 10.1021/acs.langmuir.7b03984
Langmuir 2018, 34, 4811−4819

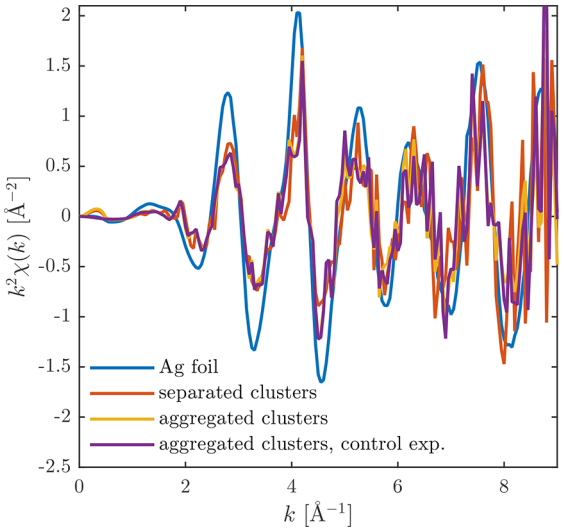

Figure 5. Ag K-edge $\chi(k)$ spectra for bulk silver foil as well as separated and aggregated Ag clusters stabilized in ionic liquid.

foil. For example, a particle with diameter ca. 40 nm should have a coordination number of ca. 11.9,[37,64] i.e., indistinguishable from bulk value.

The Ag−Ag bond of the Ag foil is slightly smaller than expected from the value determined by diffraction (2.89 Å), which can be explained by an asymmetric bond-length distribution in the first coordination shell of Ag bulk.[52] In contrast to the bulk value a reduced interatomic distance of the nearest neighbors of 2.83 ± 0.01 Å, is obtained in the sample containing separated 2 nm Ag clusters, which is in agreement with the expectation for small clusters.[67] In contrast we find for both samples containing aggregated clusters an Ag−Ag distance in the first coordination shell close to the bulk value suggesting a relaxation of the interatomic distance toward the bulk value caused by the aggregation.

The large error bars of the coordination numbers in EXAFS analysis are due to the limited k-range, available for the data fitting caused by the very low Ag concentration, even applying the fluorescence peak fitting algorithm. Changes in the cluster structure during aggregation are also observable in the XANES region as seen for the Ag clusters with the same size as used in this work, embedded in PDMS.[5] Therefore, the results found in the conventional analysis of the EXAFS data are complemented with the analysis of the XANES data using artificial neural networks (NN).[38] The algorithm is trained using theoretical Ag K-edge XANES data for Ag clusters of different size and shape calculated with the ab initio codes FEFF[57] and FDMNES.[58] As a proof for the reliability of the algorithm in an broad range of particle sizes also an Ag cluster sample prepared by DNA assisted synthesis[68,69] has been investigated. For this sample high-quality EXAFS data, measured at X18A beamline of National Synchrotron Light Source (NSLS) at Brookhaven National Laboratory, were available. In this case, EXAFS analysis results are in an excellent agreement with XANES analysis results, thus demonstrating that NN-based analysis of XANES data allows one to extract information on coordination numbers reliably.

The comparison between the results obtained using conventional EXAFS fitting and the neural network based XANES analysis is shown in Figure 7. Both methods agree within the error bars. The NN-based XANES analysis yields an increase to slightly higher coordination numbers from ca. 8 for the separated clusters to about 9 for the aggregated clusters. Furthermore, the XANES analysis is also possible for the data taken for an intermediate aggregation state with lower signal-to-noise ratio in the EXAFS region, which prohibited quantitative EXAFS analysis in this case. XANES analysis in this case yields n_1 = 8.3 ± 0.3, which is in between the results obtained for separated and aggregated clusters. Note that both EXAFS and XANES analysis suggest that for all samples the coordination numbers are significantly smaller than those in the bulk, thus

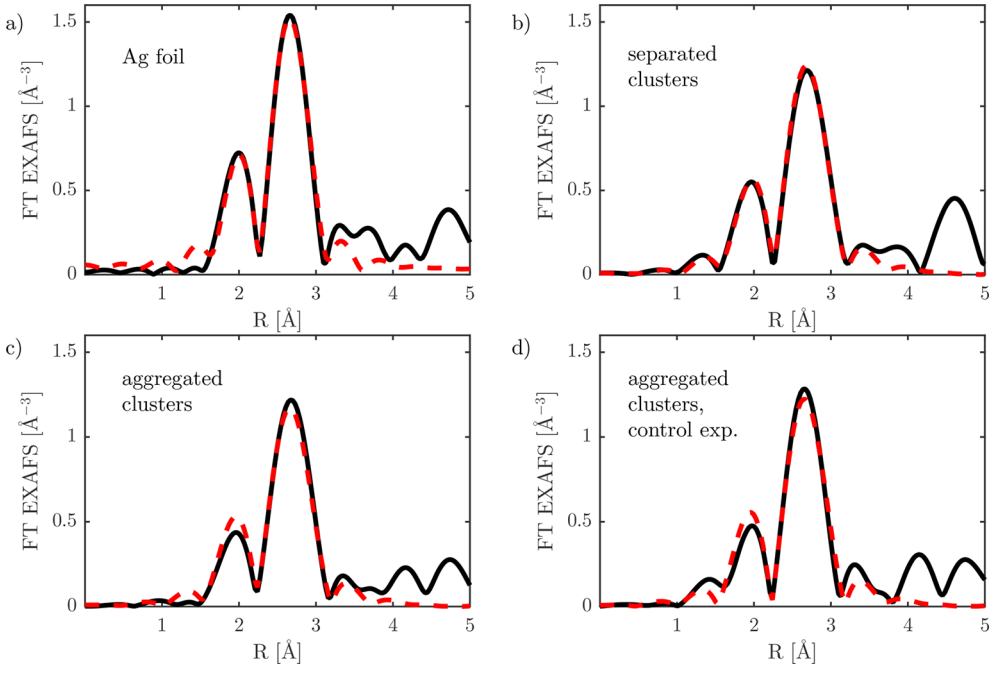

Figure 6. Fit of the first coordination shell of Ag (dashed lines) to the data (solid lines).

DOI: 10.1021/acs.langmuir.7b03984
Langmuir 2018, 34, 4811−4819

Table 1. Determination of the Structural Parameters for the Investigated XAS Spectra

	Ag foil	separated clusters	aggregated clusters	aggregated clusters, control experiment
R (Å)	2.86 ± 0.01	2.83 ± 0.01	2.86 ± 0.01	2.86 ± 0.01
σ^2 (Å^2)	0.012 ± 0.001	0.009 ± 0.001	0.008 ± 0.001	0.008 ± 0.001
C_3 ($\times 10^{-3}$ Å^3)	0.012 ± 0.001	−0.5 ± 0.2	0.1 ± 0.3	0.2 ± 0.4
n_1 (EXAFS)	12 (fixed)	9.2 ± 0.9	10.6 ± 1.1	9.0 ± 1.4
n_1 (XANES)	11.7 ± 0.2	8.0 ± 0.6	9.0 ± 0.2	8.7 ± 0.3

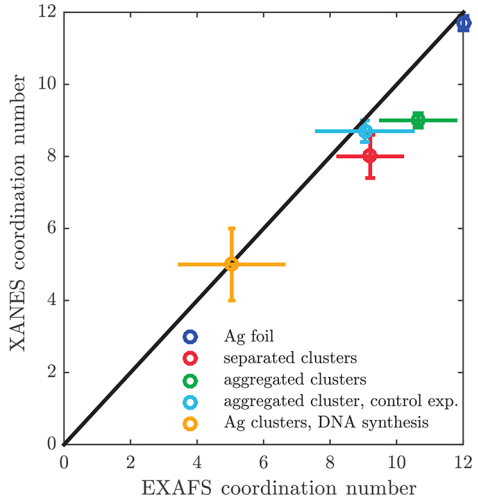

Figure 7. Comparison of the resulting coordination numbers for the first shell obtained by conventional EXAFS fitting and by applying the neural network-based XANES analysis.

the cluster size remains close to 2 nm even in the aggregated samples.

The results for the sample in which XAFS was measured before and after aggregation and for the control experiment with aggregation without previous X-ray exposure are consistent for both EXAFS and XANES analysis. We conclude therefore that sample exposure to the X-ray beam does not lead to damage of the silver cluster structures. Changes observed in the optical spectra after the X-ray exposure could be attributed to modifications in the RTIL because they also occurred for the pure RTIL.

The first-shell analysis and the determination of the first shell coordination number alone are not sufficient to determine details on the cluster shape. For well-defined particles an analysis of further coordination shells would enable the distinction between different cluster shapes (e.g., icosahedral, cubobtahedral, truncated octahedron).[64] In principle, it is possible to do such analysis using the NN-XANES method, as demonstrated in.[38] Such analysis is beyond the scope of this paper, and the interpretation of the obtained results would be difficult, because at least for aggregated samples quite broad distributions of particles shapes and sizes are expected.

CONCLUSION

We presented a detailed study on the aggregation behavior of preformed 2 nm Ag clusters deposited into the room temperature ionic liquid 1-butyl-3-methylimidazolium hexafluorophosphate. The time-dependent cluster plasmon absorption was monitored by UV/vis spectroscopy. Electrodynamic calculations using Generalized Mie Theory showed that the changes in the shape of the cluster plasmon, namely the decrease of the single particle resonance and the simultaneous increase of the extinction at lower energies can be assigned to the formation of chainlike arrangements during aggregation.

To resolve the local structure of the ionic liquid stabilized Ag clusters, we performed first coordination shell fitting of EXAFS data recorded at beamline P64 of DESY, Hamburg. With this method we can exclude the presence of large bulk-like clusters of several 10 nm diameter, which would be an alternative explanation of the changes in the optical spectra for longer time scales. The EXAFS fitting of the average first shell coordination number and the analysis of the XANES data using neural networks both show that the average coordination number only slightly increased from 8 to 9 after aggregation, meaning that the clusters still have a diameter of ca. 2 nm. Note that, nevertheless, analysis of EXAFS data suggests an increase of the Ag−Ag distance from 2.83 Å in the separated clusters to more bulk-like 2.86 Å in aggregated clusters implying some restructuring of particles.

It could be shown that sample aggregation can be significantly delayed by storing the sample at lower temperatures, which can be assigned to the extreme temperature dependency of the viscosity of C_4MIM PF_6 approaching the glass transition temperature. Using a model of diffusion limited coagulation, coagulation probabilities of $1/(1.6 \times 10^4)$ and $1/(7 \times 10^4)$ describe the experimental data for two different stages of aggregation, without further fit parameters. If the sample storage temperature is below the glass transition temperature, the aggregation process can completely be stopped. A phase transition back into the liquid state does not change the sample structure. This behavior enables sample storage on long time scales and ensures the presence of separated clusters after transferring the sample to a synchrotron radiation facility for further characterization.

The cluster plasmon analysis in combination with calculations using generalized Mie theory can also be used for other metals like gold or copper, even if the plasmon is strongest for silver. Extending the energy range, e.g., by using inelastic X-ray scattering, this approach would also be feasible for metals like aluminum or magnesium. Our method of cluster preformation in the gas phase and deposition into RTIL allows an extension to a large number of different materials and even alloys. Cluster mass selection is possible and with powerful cluster sources[10,70] a significant amount of cluster material could be deposited. For cluster materials lacking a prominent cluster plasmon the presented XAFS studies can still be performed. With the use of mass selected clusters, in particular, the NN-based XANES analysis would allow one to examine the atomistic structure of the clusters and its change due to aggregation. We already explored new in situ experiments by connecting the UV/vis cuvette and the XAFS cell in a temperature controlled circuit with a peristaltic pump. This approach for studies of cluster structure changes in situ, e.g., after adding reagents, could be a powerful tool to explore the immense new ground, which opens up in the emerging field of nanoparticles immersed in RTIL.

DOI: 10.1021/acs.langmuir.7b03984
Langmuir 2018, 34, 4811−4819

■ ASSOCIATED CONTENT

Supporting Information

The Supporting Information is available free of charge on the ACS Publications website at DOI: 10.1021/acs.langmuir.7b03984.

Time- and temperature-dependent UV/vis absorption measurement series for the three storage temperatures as well as pictures taken for visual appearance of the aggregation process (PDF)

■ AUTHOR INFORMATION

Corresponding Author

*E-mail: heinz.hoevel@tu-dortmund.de.

ORCID

Stefanie Roese: 0000-0002-2396-6954

Anatoly I. Frenkel: 0000-0002-5451-1207

Notes

The authors declare no competing financial interest.

■ ACKNOWLEDGMENTS

Parts of this research were carried out at P64 at DESY, a member of the Helmholtz Association (HGF). We thank V. Murzi, L. M. Martín-Montoya, and W. Caliebe for assistance in using beamline P64. A first precharacterization of the samples by XANES measurements was performed at the Ag L_3 edge at BL8, DELTA, Technische Universität Dortmund, Germany. A.I.F.'s work was funded by the Division of Chemical Sciences, Geosciences, and Biosciences, Office of Basic Energy Sciences of the U.S. Department of Energy through Grant DE-FG02-03ER15476. The authors thank Dr. D. Nykypanchuk from the Center for Functional Nanomaterials at Brookhaven National Laboratory for providing the Ag sample prepared by DNA templated synthesis. This research used resources of the Center for Functional Nanomaterials, which is a U.S. DOE Office of Science Facility, and beamline X18A of the National Synchrotron Light Source at Brookhaven National Laboratory under Contract DE-SC0012704.

■ REFERENCES

(1) Astruc, D.; Lu, F.; Aranzaes, J. R. *Angew. Chem., Int. Ed.* **2005**, *44*, 7852−7872.

(2) Shipway, A. N.; Katz, E.; Willner, I. *ChemPhysChem* **2000**, *1*, 18−52.

(3) Jiang, N.; Ruan, Q.; Qin, F.; Wang, J.; Lin, H.-Q. *Nanoscale* **2015**, *7*, 12516−26.

(4) Ghisleri, C.; Borghi, F.; Ravagnan, L.; Podesta, A.; Melis, C.; Colombo, L.; Milani, P. *J. Phys. D: Appl. Phys.* **2014**, *47*, 015301.

(5) Roese, S.; Engemann, D.; Hoffmann, S.; Latussek, K.; Sternemann, C.; Hövel, H. *J. Phys.: Conf. Ser.* **2016**, *712*, 012068.

(6) Bahena, D.; Bhattarai, N.; Santiago, U.; Tlahuice, A.; Ponce, A.; Bach, S. B. H.; Yoon, B.; Whetten, R. L.; Landman, U.; Jose-Yacaman, M. *J. Phys. Chem. Lett.* **2013**, *4*, 975−981.

(7) Wang, B.; Yoon, B.; König, M.; Fukamori, Y.; Esch, F.; Heiz, U.; Landman, U. *Nano Lett.* **2012**, *12*, 5907−5912.

(8) Degen, S.; Becker, C.; Wandelt, K. *Faraday Discuss.* **2004**, *125*, 343.

(9) Duffe, S.; Irawan, T.; Bieletzki, M.; Richter, T.; Sieben, B.; Yin, C.; Von Issendorff, B.; Moseler, M.; Hövel, H. *Eur. Phys. J. D* **2007**, *45*, 401−408.

(10) Jian, N.; Bauer, K.; Palmer, R. E. *Nanotechnology* **2017**, *28*, 325601.

(11) Grönhagen, N.; Järvi, T. T.; Miroslawski, N.; Hövel, H.; Moseler, M. *J. Phys. Chem. C* **2012**, *116*, 19327−19334.

(12) Van Lith, J.; Lassesson, A.; Brown, S. A.; Schulze, M.; Partridge, J. G.; Ayesh, A. *Appl. Phys. Lett.* **2007**, *91*, 181910.

(13) Corbelli, G.; Ghisleri, C.; Marelli, M.; Milani, P.; Ravagnan, L. *Adv. Mater.* **2011**, *23*, 4504−4508.

(14) Bryckaert, M.; Kharchenko, A.; Lebedev, O.; Dong, B.; De Waele, I.; Buntinx, G.; Poizat, O.; Mintova, S.; De Waele, V. *J. Phys. Chem. C* **2017**, *121*, 26958−26966.

(15) Kim, S. M.; Lee, S. W.; Moon, S. Y.; Park, J. Y. *J. Phys.: Condens. Matter* **2016**, *28*, 254002.

(16) Shen, Y.; Cheng, X.; Li, G.; Zhu, Q.; Chi, Z.; Wang, J.; Jin, C. *Nanoscale Horiz.* **2016**, *1*, 290−297.

(17) Radziuk, D.; Moehwald, H. *Phys. Chem. Chem. Phys.* **2015**, *17*, 21072−21093.

(18) Hartland, G. V.; Besteiro, L. V.; Johns, P.; Govorov, A. O. *ACS Energy Letters* **2017**, *2*, 1641−1653.

(19) Kraynov, A.; Müller, T. E. *Applications of Ionic Liquids in Science and Technology*; InTech Open: Rijeka, Croatia, 2011; pp 235−260.

(20) Freemantle, M. *An Introduction to Ionic Liquids*; RSC Publishing: London, 2010.

(21) Dupont, J.; Fonseca, G. S.; Umpierre, A. P.; Fichtner, P. F. P.; Teixeira, S. R. *J. Am. Chem. Soc.* **2002**, *124*, 4228−4229.

(22) Guo, S.; Shi, F.; Gu, Y.; Yang, J.; Deng, Y. *Chem. Lett.* **2005**, *34*, 830−831.

(23) Suzuki, T.; Okazaki, K.-i.; Kiyama, T.; Kuwabata, S.; Torimoto, T. *Electrochemistry* **2009**, *77*, 636−638.

(24) Vanecht, E.; Binnemans, K.; Seo, J. W.; Stappers, L.; Fransaer, J. *Phys. Chem. Chem. Phys.* **2011**, *13*, 13565−13571.

(25) Wender, H.; de Oliveira, L. F.; Migowski, P.; Feil, A. F.; Lissner, E.; Prechtl, M. H. G.; Teixeira, S. R.; Dupont, J. *J. Phys. Chem. C* **2010**, *114*, 11764−11768.

(26) Richter, K.; Birkner, A.; Mudring, A.-V. *Angew. Chem., Int. Ed.* **2010**, *49*, 2431−2435.

(27) Dupont, J.; Scholten, J. D. *Chem. Soc. Rev.* **2010**, *39*, 1780−1804.

(28) Richter, K.; Birkner, A.; Mudring, A.-V. *Phys. Chem. Chem. Phys.* **2011**, *13*, 7136−7141.

(29) Zhu, J.; Shen, Y.; Xie, A.; Qiu, L.; Zhang, Q.; Zhang, S. *J. Phys. Chem. C* **2007**, *111*, 7629−7633.

(30) Okazaki, K.-i.; Kiyama, T.; Hirahara, K.; Tanaka, N.; Kuwabata, S.; Torimoto, T. *Chem. Commun.* **2008**, 691−693.

(31) Kim, K.-S.; Choi, S.; Cha, J.-H.; Yeon, S.-H.; Lee, H. *J. Mater. Chem.* **2006**, *16*, 1315.

(32) Itoh, H.; Naka, K.; Chujo, Y. *J. Am. Chem. Soc.* **2004**, *126*, 3026−3027.

(33) Schrekker, H. S.; Gelesky, M. A.; Stracke, M. P.; Schrekker, C. M.; Machado, G.; Teixeira, S. R.; Rubim, J. C.; Dupont, J. *J. Colloid Interface Sci.* **2007**, *316*, 189−195.

(34) Wang, Y.; Yang, H. *Chem. Commun.* **2006**, 2545.

(35) Vanecht, E.; Binnemans, K.; Patskovsky, S.; Meunier, M.; Seo, J. W.; Stappers, L.; Fransaer, J. *Phys. Chem. Chem. Phys.* **2012**, *14*, 5662−5671.

(36) Engemann, D. C.; Roese, S.; Hövel, H. *J. Phys. Chem. C* **2016**, *120*, 6239−6245.

(37) Frenkel, A. I.; Yevick, A.; Cooper, C.; Vasic, R. *Annu. Rev. Anal. Chem.* **2011**, *4*, 23−39.

(38) Timoshenko, J.; Lu, D.; Lin, Y.; Frenkel, A. I. *J. Phys. Chem. Lett.* **2017**, *8*, 5091−5098.

(39) Hövel, H.; Fritz, S.; Hilger, A.; Kreibig, U.; Vollmer, M. *Phys. Rev. B: Condens. Matter Mater. Phys.* **1993**, *48*, 18178−18188.

(40) Kreibig, U.; Vollmer, M. *Optical Properties of Metal Clusters*; Springer−Verlag: Berlin, 1995.

(41) Gérardy, J. M.; Ausloos, M. *Phys. Rev. B: Condens. Matter Mater. Phys.* **1982**, *25*, 4204−4229.

(42) Pellegrini, G.; Mattei, G.; Bello, V.; Mazzoldi, P. *Mater. Sci. Eng., C* **2007**, *27*, 1347−1350.

(43) Quinten, M. *Optical Properties of Nanoparticle Systems*; Wiley−VCH: Weinheim, Germany, 2011.

(44) Johnson, P. B.; Christy, R. W. *Phys. Rev. B* **1972**, *6*, 4370−4379.

(45) Quinten, M.; Kreibig, U. *Appl. Opt.* **1993**, *32*, 6173−6182.

DOI: 10.1021/acs.langmuir.7b03984
Langmuir 2018, 34, 4811−4819

(46) Dash, P.; Miller, S. M.; Scott, R. W. *J. Mol. Catal. A: Chem.* **2010**, *329*, 86−95.
(47) Harris, K. R.; Woolf, L. A.; Kanakubo, M. *J. Chem. Eng. Data* **2005**, *50*, 1777−1782.
(48) Fredlake, C. P.; Crosthwaite, J. M.; Hert, D. G.; Aki, S. N. V. K.; Brennecke, J. F. *J. Chem. Eng. Data* **2004**, *49*, 954−964.
(49) Rehr, J. J.; Albers, R. C. *Rev. Mod. Phys.* **2000**, *72*, 621−654.
(50) Clausen, B. S.; Nørskov, J. K. *Top. Catal.* **2000**, *10*, 221−230.
(51) Chill, S. T.; Anderson, R. M.; Yancey, D. F.; Frenkel, A. I.; Crooks, R. M.; Henkelman, G. *ACS Nano* **2015**, *9*, 4036−4042.
(52) Timoshenko, J.; Frenkel, A. I. *Catal. Today* **2017**, *280*, 274−282.
(53) Witkowska, A.; Di Cicco, A.; Principi, E. *Phys. Rev. B: Condens. Matter Mater. Phys.* **2007**, *76*, 104110.
(54) Ankudinov, A. L.; Ravel, B.; Rehr, J. J.; Conradson, S. D. *Phys. Rev. B: Condens. Matter Mater. Phys.* **1998**, *58*, 7565−7576.
(55) Ankudinov, A.; Rehr, J.; Low, J.; Bare, S. *Top. Catal.* **2002**, *18*, 3−7.
(56) Bazin, D.; Sayers, D.; Rehr, J. J.; Mottet, C. *J. Phys. Chem. B* **1997**, *101*, 5332−5336.
(57) Rehr, J. J.; Kas, J. J.; Vila, F. D.; Prange, M. P.; Jorissen, K. *Phys. Chem. Chem. Phys.* **2010**, *12*, 5503.
(58) Joly, Y. *Phys. Rev. B: Condens. Matter Mater. Phys.* **2001**, *63*, 125120.
(59) Tamenori, Y.; Morita, M.; Nakamura, T. *J. Synchrotron Radiat.* **2011**, *18*, 747−752.
(60) Martín-Montoya, L. A.; Rothkirch, A.; Caliebe, W. *J. Phys.: Conf. Ser.* **2016**, *712*, 012016.
(61) Newville, M.; Ravel, B.; Haskel, D.; Rehr, J.; Stern, E.; Yacoby, Y. *Phys. B* **1995**, *208−209*, 154−156.
(62) Newville, M. *J. Phys.: Conf. Ser.* **2013**, *430*, 012007.
(63) Ravel, B. *J. Alloys Compd.* **2005**, *401*, 118−126.
(64) Glasner, D.; Frenkel, A. I. Geometrical Characteristics of Regular Polyhedra: Application to EXAFS Studies of Nanoclusters. *AIP Conf. Proc.* **2007**, *882*, 746−748.
(65) Jentys, A. *Phys. Chem. Chem. Phys.* **1999**, *1*, 4059−4063.
(66) Price, S. W. T.; Zonias, N.; Skylaris, C.-K.; Hyde, T. I.; Ravel, B.; Russell, A. E. *Phys. Rev. B: Condens. Matter Mater. Phys.* **2012**, *85*, 075439.
(67) Apai, G.; Hamilton, J. F.; Stohr, J.; Thompson, A. *Phys. Rev. Lett.* **1979**, *43*, 165−169.
(68) Gwinn, E. G.; O'Neill, P.; Guerrero, A. J.; Bouwmeester, D.; Fygenson, D. K. *Adv. Mater.* **2008**, *20*, 279−283.
(69) O'Neill, P. R.; Velazquez, L. R.; Dunn, D. G.; Gwinn, E. G.; Fygenson, D. K. *J. Phys. Chem. C* **2009**, *113*, 4229−4233.
(70) Palmer, R. E.; Cao, L.; Yin, F. *Rev. Sci. Instrum.* **2016**, *87*, 046103.

DOI: 10.1021/acs.langmuir.7b03984
Langmuir 2018, 34, 4811−4819